THE JOURNAL OF PHYSICAL CHEMISTRY B
A JOURNAL OF THE AMERICAN CHEMICAL SOCIETY

pubs.acs.org/JPCB

Article

Microscopic Solvation Dynamics and Transport in LiFSA-Sulfone Electrolytes via Optimized Force Fields: A Classical MD Perspective

Published as part of The Journal of Physical Chemistry B special issue "Athanassios Z. Panagiotopoulos Festschrift".

Yati and Anirban Mondal*

Cite This: https://doi.org/10.1021/acs.jpcb.5c02097

Read Online

ACCESS | Metrics & More | Article Recommendations | Supporting Information

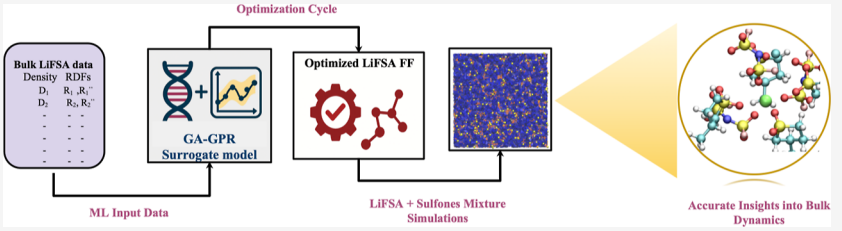

ABSTRACT: Lithium bis(fluorosulfonyl)amide (LiFSA) is a commonly used lithium salt in electrolyte formulations due to its electrochemical stability, favorable ionic dissociation, and potential for enhancing lithium-ion transport in energy storage applications. Understanding the solvation dynamics and transport properties of LiFSA, particularly in mixtures with sulfone-based solvents, is crucial for optimizing electrolyte performance. Accurate force field parametrization is essential for simulating complex electrolyte systems with reliable predictive power. This study presents a robust workflow combining a genetic algorithm (GA) and Gaussian process regression (GPR) to develop optimized Lennard-Jones parameters for pure LiFSA, which are subsequently transferred to LiFSA-sulfone mixtures. The optimized parameters accurately capture nonbonded interactions and reproduce experimental transport properties, including viscosity and ionic conductivity, with deviations within 7.5%. Using the Green−Kubo formalism, viscosity and conductivity trends were computed and linked to solvation dynamics, revealing that mixtures containing symmetric sulfones (sulfolane and dimethyl sulfone) exhibit lower viscosities and higher conductivities compared to those with asymmetric sulfones (ethyl methyl sulfone and 3-methyl sulfolane). Analysis of relative coordination numbers further demonstrates the pivotal role of solvent oxygen (O_S) in modulating ion transport, with enhanced O_S coordination reducing viscosity and improving conductivity by facilitating ion mobility. This study provides a microscopic understanding of how ion−solvent interactions and solvation structures govern macroscopic transport behavior. The GA-GPR parametrization framework not only delivers transferable force fields capable of accurately predicting electrolyte properties but also offers practical insights for tailoring electrolytes with optimized performance in energy storage and conversion applications.

1. INTRODUCTION

Lithium-ion batteries (LiBs) are pivotal in portable electronics and renewable energy storage owing to their high energy density, long cycle life, and efficiency.[1−3] The electrolyte, a critical component of LiBs, governs ion transport, stability, and overall battery performance. Designing efficient electrolytes requires balancing multiple factors, including fast cation diffusion, resistance to side reactions, high thermal stability, and extended charge−discharge cycle life.[2,4] Typically composed of a lithium salt [e.g., lithium bis(fluorosulfonyl)-amide, LiFSA] dissolved in a solvent or solvent mixture, electrolytes' properties are significantly influenced by solvent choice and concentration, necessitating a detailed molecular-level understanding of these systems.[5−8] Sulfone-based solvents have emerged as promising candidates for high-performance LiB electrolytes due to their high dielectric constant and electrochemical stability.[4,9−11] Both aliphatic (e.g., dimethyl sulfone, DMS, and ethyl methyl sulfone, EMS) and cyclic (e.g., sulfolane, SL, and 3-methyl sulfolane, MSL) sulfones exhibit distinct solvation behaviors. Their symmetric (DMS, SL) or asymmetric (EMS, MSL) molecular structures further influence the physicochemical properties of electrolyte mixtures.[4,9,12−16]

Classical molecular dynamics (MD) simulations offer a powerful tool to probe electrolyte dynamics at the atomic

Received: March 28, 2025
Revised: May 29, 2025
Accepted: June 23, 2025

level.[9,17−20] However, the accuracy of these simulations critically depends on the choice of force field, which defines bonded and nonbonded interactions. While generally applicable, standard force fields are not specifically optimized for LiFSA-sulfone mixtures, often leading to inaccuracies in capturing charge distributions and van der Waals interactions. These limitations can affect key electrolyte properties such as viscosity, conductivity, and ion diffusion. Notably, no specific force fields are available for LiFSA, and existing force fields like OPLS[21,22] are incapable of predicting correct dynamics, often resulting in sluggish ion transport.[9,23] Therefore, developing an accurate force field for LiFSA is crucial before investigating mixture properties.

To address these challenges, we developed a novel force field parametrization approach tailored to the individual components of these electrolyte mixtures.[24] Our method integrates a genetic algorithm (GA) with Gaussian process regression (GPR) in an active learning framework, significantly reducing the computational cost compared to conventional manual tuning[15,25−27] or machine learning-based optimization methods.[28−32] This approach achieved convergence in just seven iterations using only 275 data points, demonstrating its efficiency and potential for broader applications in electrolyte modeling. Initially developed in our previous work[24] to obtain accurate force field parameters for all four sulfones, this method demonstrated precise predictions of viscosity, surface tension, liquid phase density, and radial distribution functions (RDFs), validated against experimental data[24] and ab initio MD (AIMD) trajectories. In the present study, we first apply this framework to optimize force field parameters for LiFSA and validate them against available reference data. Recent QM-to-MM mapping methods provide physically motivated force field parameters derived directly from quantum electron density partitioning.[33,34] Our approach differs by combining genetic algorithm−guided global optimization with Gaussian process regression to iteratively refine parameters based on condensed-phase properties. This data-driven strategy complements deterministic atom-in-molecule (AIM) mappings by enabling the correction of QM-derived parameters to capture experimental observables better, improving accuracy and transferability for complex chemical families such as sulfone additives.

This study focuses on binary mixtures of LiFSA with four sulfone solvents (SL, MSL, DMS, and EMS) in a 1:3 salt-to-solvent molar ratio. Using our optimized force fields for both LiFSA (developed in this work) and sulfones (from our previous study),[24] we conducted MD simulations to investigate how molecular interactions at the atomic scale dictate the structural and transport properties of these mixtures. We validated our simulation results against experimental density and transport properties,[4] ensuring accurate capture of key electrolyte behaviors. Further analysis of solvation structure and molecular organization was performed using radial distribution functions, angular distributions, rotational autocorrelation functions (RACFs), and coordination number calculations.

The novelty of this work lies in several key aspects. We present the development of an accurate force field for LiFSA using a robust active learning approach. This study offers a comprehensive investigation of LiFSA-sulfone binary mixtures using optimized force fields for both the salt and solvents, elucidating the influence of aliphatic vs cyclic sulfones and symmetric vs asymmetric solvent structures on Li-ion solvation and transport. By providing these insights, this study contributes to a deeper understanding of sulfone-based solvents' potential in next-generation LiB electrolytes and paves the way for more accurate and efficient modeling of complex electrolyte systems.

2. METHODS

In this study, we developed a robust and accurate force field for lithium LiFSA using the OPLS functional form,[21,22] building upon our previous work with sulfone molecules.[24] The force field describes intramolecular and intermolecular interactions through bonded and nonbonded terms. The total potential energy (U_{total}) for the system is expressed as

$$U_{total} = \sum_{bonds} k_b(r - r_0)^2 + \sum_{angles} k_\theta(\theta - \theta_0)^2 + \sum_{dihedrals} \sum_{n=0}^{5} C_n \cos^n(\phi) + \sum_{i<j} \left[4\epsilon_{ij} \left(\left(\frac{\sigma_{ij}}{r_{ij}} \right)^{12} - \left(\frac{\sigma_{ij}}{r_{ij}} \right)^{6} \right) + \frac{q_i q_j}{4\pi\epsilon_0 r_{ij}} \right]$$

In this equation, the bonded interactions include terms for bonds, angles, and dihedrals, while nonbonded interactions are represented by Lennard-Jones (LJ) potentials and electrostatic interactions. The Ryckaert-Bellemans coefficients (C_n) allow for a flexible representation of dihedral interactions, which is crucial for capturing the conformational behavior of the FSA anion. For LiFSA, we adopted the intramolecular bonded parameters directly from ref 25. However, the partial charges required special attention due to the ionic nature of LiFSA. Atomic partial charges for LiFSA were derived using the DDEC6 method,[35] implemented in Chargemol,[36] applied to the gas-phase DFT-optimized structure of the isolated ion pair. Although periodic systems can also be used for charge derivation, the gas-phase model was chosen to balance physical accuracy with computational efficiency. The optimization was performed at the M06−2X/aug-cc-pVDZ level of theory using the Gaussian 09 program.[37] This approach ensured a balanced representation of the charge distribution within the ionic compound and was consistently applied across all pure and mixed systems. The reliability of these charges is supported by the good agreement between calculated and experimental dielectric properties observed in our previous work.[24]

We aimed to estimate optimal values using reference data for the nonbonded interactions, particularly the LJ parameters σ and ϵ (see Figure 1 for atom type definition). The unlike

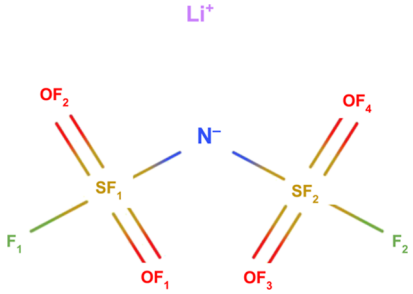

Figure 1. Molecular structure and atom types of LiFSA used in this study.

https://doi.org/10.1021/acs.jpcb.5c02097
J. Phys. Chem. B XXXX, XXX, XXX−XXX

interactions between atom types were calculated using the Lorentz−Berthelot combining rules. The optimization of these parameters was guided primarily by two reference quantities: the liquid phase density of LiFSA and site-specific radial distribution functions, focusing on key atom pairs such as Li−O and O−O. Due to the lack of available experimental data for the density of pure LiFSA in its molten state, we relied on ab initio molecular dynamics simulations to obtain reference density values for force field parametrization. Despite an extensive literature search, we found no reported experimental measurements for neat LiFSA density, typically limited to its mixtures with solvents. These AIMD simulations provided density estimates and the trajectories necessary to compute accurate RDFs, offering a detailed picture of the molecular structure and interactions in the liquid phase. This approach ensures a consistent and physically grounded force field for LiFSA that is compatible with our previously developed force fields for sulfone molecules[24] while accounting for the unique characteristics of this ionic compound.

2.1. Reference Database Generation. *2.1.1. Ab Initio Molecular Dynamics Simulations.* We conducted AIMD simulations of LiFSA in the liquid state to obtain reference values for the fitness calculation. The initial configuration was constructed using the optimized ground-state geometry of LiFSA. We packed 30 LiFSA ion pairs into a cubic box with a side length of approximately 20 Å using Packmol.[38] This system size was chosen to balance computational cost with an adequate sampling of the ionic liquid structure. Before the AIMD run, we performed classical molecular dynamics simulations using GROMACS v2020.4[39,40] to equilibrate the system. Starting from an energy-minimized configuration, we simulated a cubic box containing 30 LiFSA ion pairs with periodic boundary conditions applied in all directions. The system evolved for 1 ns in the *NPT* ensemble using a time step of 1 fs. Temperature was maintained at 423 K using the velocity-rescaling thermostat,[41] and pressure was kept at 1 bar using the Berendsen barostat.[42] Electrostatic interactions were treated with the smooth particle mesh Ewald (SPME) method,[43] and a cutoff of 1.3 nm was applied for both Coulombic and van der Waals interactions. This equilibration ensured the system attained a realistic density prior to AIMD. The resulting supercell was then geometry optimized within the density functional theory (DFT) framework. We set convergence criteria of 10^{-6} and 10^{-5} au for the gradients on the wave functions and nuclear positions, respectively. The other important DFT parameters were kept the same, as discussed below. Since the system undergoes extensive equilibration, the final density obtained from AIMD is not sensitive to the specific choice of initial configuration.

We performed Born−Oppenheimer MD simulations using the Quickstep module[44,45] of the CP2K electronic structure code.[46] The AIMD simulations employed density functional theory within the Gaussian and plane wave (GPW) framework. We used the Perdew−Burke−Ernzerhof (PBE)[47] functional to account for exchange−correlation effects, supplemented with Grimme's D3[48] empirical dispersion correction to capture long−range interactions, crucial for ionic liquids. We set the dispersion cutoff to 16 Å. For the wave function calculations, we employed double ζ valence polarization (DZVP) basis sets with short-range terms for each atom type, using an energy cutoff of 500 Ry. The norm-conserving Goedecker−Teter−Hutter (GTH)[49,50] pseudopotentials were applied to consider the effect of nuclei and core electrons. We integrated the equations of motion with a time step of 1 fs. The system was equilibrated for 50 ps in the *NPT* ensemble at 1 bar using an isotropic unit cell according to the Martyna et al. scheme,[51] with a time constant of 500 fs. Following equilibration, we conducted a production simulation in the canonical *NVT* ensemble for 20 ps. The temperature was set at 423 K, above the melting point of LiFSA 403 K[4], and controlled by one chain of six Nosé−Hoover thermostats[52] with a time constant of 100 fs. We employed three-dimensional periodic boundary conditions in all simulations. We stored the trajectory every 10 fs for postsimulation analysis. We computed radial distribution functions from these trajectories for key atom pairs, including Li−O and O−O. The final set of liquid phase densities and these RDFs served as reference data for our machine learning model, providing a benchmark to optimize the force field parameters for LiFSA efficiently.

2.1.2. Classical Molecular Dynamics Simulations. To develop the Gaussian process regression surrogate model for LiFSA, we generated a training data set through a series of classical MD simulations. A detailed workflow is displayed in Figure S1 in the Supporting Information. The initial force field was constructed using the OPLS functional form[21,22] for nonbonded interactions and bonded parameters from ref 25, with atomic site charges determined via the DDEC6 method,[35] yielding a parent parameter set. We employed a genetic algorithm to explore the nonbonded Lennard-Jones parameter space by introducing ±5% perturbations to the σ and ϵ values of selected atom types in Li^+ and FSA^- ion. Each mutation generated 200 offspring parameter sets per generation, enabling efficient sampling and optimization of the LJ interaction parameters. We performed classical MD simulations on systems containing 1000 LiFSA ion pairs using these 200 mutated parameter sets. The simulations were conducted using the GROMACS v2020.4[39,40] engine under thermodynamic conditions matching those of the AIMD simulations to achieve equilibrated configurations. We initialized the simulations from energetically minimized configurations and employed a time step of 1 fs. The simulations used a cubic box with periodic boundary conditions applied in all directions. We conducted the simulations in the *NPT* ensemble, utilizing a velocity-rescaling thermostat[41] to maintain the temperature at 423 K and a Berendsen barostat[42] to control pressure at 1 bar. For electrostatic interactions, we employed the smooth particle mesh Ewald (SPME) method[43] for real-space calculations and fast Fourier transform (FFT) for reciprocal lattice points. We set the cutoff for Coulombic and van der Waals interactions to 1.3 nm. Each simulation was run for 2 ns, with the first 500 ps treated as equilibration. Densities were computed from the final 1 ns of the trajectory to ensure accurate sampling of the equilibrated state.

For each of the 200 parameter sets, we calculated the liquid phase density and radial distribution functions for key atom pairs, including Li−O and O−O, once volume equilibration was achieved. These computed densities and RDFs constituted the training and testing data for the GPR surrogate model, providing the necessary input to optimize the force field parameters for LiFSA. The optimization was performed using the full radial distribution functions as target properties to ensure a comprehensive and transferable description of the solvation structure. This approach captures both short- and medium-range correlations beyond the first solvation shell, which are often inadequately represented when using only select RDF features such as peak positions or coordination

https://doi.org/10.1021/acs.jpcb.5c02097
J. Phys. Chem. B XXXX, XXX, XXX−XXX

numbers. Moreover, key structural descriptors—such as the coordination number—are inherently encoded in the full RDF through integration, allowing for physically consistent optimization. This continuous representation also facilitates smoother convergence in the GA-GPR workflow and enhances the robustness of the optimized force field when applied to mixture systems. This approach allowed for a comprehensive exploration of the parameter space, facilitating the development of an accurate and efficient force field tailored for LiFSA.

2.2. Optimization Workflow. *2.2.1. Fitness Function for LJ Parameter Optimization.* To evaluate how well the predicted force fields reproduce the reference liquid phase properties of LiFSA, we defined a fitness function that quantifies the deviation between predicted values and reference data. The overall fitness function, F, was designed to simultaneously minimize the error in density and the deviation in RDFs

$$F = w_{\text{density}}F_{\text{density}} + w_{\text{RDF}}F_{\text{RDF}} \tag{1}$$

where w_{density} and w_{RDF} are weights accounting for the different units and magnitudes of the two components. The density component, F_{density}, represents the absolute error between predicted and reference densities

$$F_{\text{density}} = |D_{\text{FF}} - D_{\text{Ref.}}| \tag{2}$$

Here, D_{FF} is the density obtained from classical MD simulations using the predicted force field, and $D_{\text{ref.}}$ is the reference density from AIMD simulations. The RDF component, F_{RDF}, calculates the root-mean-square error between predicted and reference RDFs for key atom pairs in LiFSA

$$F_{\text{RDF}} = \sqrt{\frac{\chi^2_{\text{LiO}} + \chi^2_{\text{OO}}}{2}} \tag{3}$$

The terms χ^2_{LiO} and χ^2_{OO} quantify the deviation between the predicted and reference RDFs and are computed as follows.

$$\chi^2_{\alpha\alpha} = \frac{\sum_r [g^{\text{AIMD}}_{\alpha\alpha}(r) - g^{\text{MD}}_{\alpha\alpha}(r)]^2}{\sum_r [g^{\text{AIMD}}_{\alpha\alpha}(r)]^2} \tag{4}$$

where $g^{\text{AIMD}}_{\alpha\alpha}(r)$ and $g^{\text{MD}}_{\alpha\alpha}(r)$ are the RDFs for atom pairs α-α (Li−O or O−O), and r is the distance over which RDFs were calculated, ranging from 0.0 to 9.0 Å, with a spacing of 0.02 Å. This fitness function reduces the task of determining optimal force field parameters to an optimization problem, aiming to minimize F by adjusting the nonbonding parameters σ and ϵ. This ensures accurate reproduction of both structural (RDF) and thermodynamic (density) properties of LiFSA. Further details on implementing this fitness function can be found in our previous work.[24] Figure S1 summarizes the entire optimization workflow.

2.2.2. Surrogate Model and Optimization Process. Our optimization process employed a Gaussian process regression model as a surrogate to predict fitness values for different Lennard-Jones parameter sets. This model was integrated into a genetic algorithm framework, forming an active learning loop to search for optimized parameters efficiently. The GPR model, implemented using the `Scikit-learn`[53] library, uses a composite kernel function combining a constant kernel and a Radial Basis Function (RBF) kernel. This configuration allows the model to capture both global variance and local smoothness in the fitness landscape. The model's hyperparameters were optimized through 10 restarts to ensure robust training.

The GA, developed using the `DEAP`[54] library, systematically explores the LJ parameter space. It generates new candidate sets through mutation and crossover operations, with initial bounds set within ±5% of OPLS nonbonded parameters. These bounds were later expanded based on observed parameter ranges in the initial data set. The active learning process involves iterative refinement of the GPR model. In each iteration, the GA generates 500 new candidate parameters; the GPR model predicts their fitness, and the top 10−15 candidates undergo classical MD simulations for actual fitness evaluation. These new data points are then added to the training data set, and the GPR model is retrained. This process typically converged after 7 iterations, resulting in a data set of approximately 275 points. The parameter set with the lowest fitness value from the final iteration was selected as the optimal force field, with minor manual adjustments for fine-tuning if necessary. Other specific details of the surrogate model and optimization process, including kernel function parameters, GA operations, and convergence criteria, were kept consistent with our previous work.[24] This approach ensures an efficient and reliable optimization of force field parameters for LiFSA, building upon our established methodology.

2.3. Production Simulation. Production simulations for pure LiFSA and its mixtures were performed using classical molecular dynamics with the GA-GPR optimized force field. For pure LiFSA, an energy-minimized configuration consisting of 3000 LiFSA molecules at 423 K was equilibrated in the *NPT* ensemble using a time step of 1 fs. The total duration of the simulation was 50 ns. An identical simulation was also conducted using the OPLS force field for comparison. These simulations used a 1.3 nm cutoff for long−range interactions, with temperature and pressure controlled by a velocity-rescaling thermostat[41] and Berendsen barostat,[42] respectively. Due to the limited availability of experimental data on the transport properties of pure LiFSA, the comparison between GA-GPR and OPLS force fields was based on structural observables—specifically, the equilibrium density and radial distribution functions derived from the equilibrated trajectories.

Mixture simulations maintained a 1:3 molar ratio of salt-to-solvent at 303 K. This ratio of salt-to-solvent was based on experimental measurements, allowing for direct comparison between our simulations and experimental results.[4] The force fields for sulfones were taken from our previous work, which used the same GA-GPR surrogate model.[24] Simulations were performed in the *NPT* ensemble for 10 ns equilibration with a 1 fs time step, using a Berendsen barostat[42] and velocity rescaling[41] for temperature control. The LiFSA-SL mixture required an additional 5 ns for equilibration. Two independently equilibrated configurations were used for the *NVT* production runs to improve statistical accuracy in transport property calculations. Each 5 ns production trajectory was segmented into multiple statistically independent blocks to compute transport properties such as viscosity and ionic conductivity.

To benchmark the performance of the GA-GPR force field, we also performed NPT simulations for each mixture using the standard OPLS force field. The resulting densities were compared with experimental values to assess the relative performance of the two models. This comparison highlights the improvement offered by the GA-GPR parameters. We want

https://doi.org/10.1021/acs.jpcb.5c02097
J. Phys. Chem. B XXXX, XXX, XXX−XXX

to note that we have limited the comparison to density due to the high computational cost associated with transport property calculations (which require long simulation trajectories and careful statistical averaging). However, in our previous work [ref 24], we performed a detailed assessment of OPLS-based transport properties for pure sulfone systems and found considerable discrepancies with experimental viscosity and conductivity values. These observations reinforce the advantage of the GA-GPR force field in delivering improved accuracy for both structural and transport properties compared to the conventional OPLS force field.

To validate the developed force fields, we computed the viscosity (η) of each mixture using the Green−Kubo relation, which involves integrating the pressure autocorrelation function.[55−57] The viscosity is given by

$$\eta = \frac{V}{k_B T} \int_0^\infty \langle P_{\alpha\beta}(0) P_{\alpha\beta}(t) \rangle \, dt \tag{5}$$

where V is the simulation volume and $(P_{\alpha\beta})$ represents the pressure tensor components. We recorded the pressure tensor after every 10 fs steps to accurately capture the short-time behavior of the autocorrelation function. The integral in eq 5 converged after 100 ps for aliphatic sulfones and 150 ps for cyclic sulfone mixtures. Running integrals of the stress autocorrelation function were evaluated over correlation lengths ranging from 175 to 250 ps, with offset times of 20 ps, resulting in approximately 20 independent segments. The final reported viscosities were obtained by averaging the cumulative integral over the converged viscosities, ensuring robust and statistically significant results. Error bars were computed using block averaging across these segments.

The Green−Kubo method for calculating ionic conductivity (σ) involves integrating the current autocorrelation function over time

$$\sigma = \frac{1}{3Vk_B T} \int_0^\infty \vec{j}(0) \cdot \vec{j}(t) \, dt \tag{6}$$

where V is the system volume, k_B is the Boltzmann constant, T is the temperature, and $\vec{j}$ is the electric current vector. This method directly accounts for correlated ion motions and provides a more accurate representation of ionic conductivity in complex electrolyte systems. The current autocorrelation function was integrated over correlation times of approximately 7 ps with a 20 ps offset, yielding around 500 independent segments. The final conductivity reported was averaged over the last 3 ps. Error bars were computed using block averaging across these segments.

3. RESULTS AND DISCUSSION

3.1. Pure LiFSA. The optimization of Lennard-Jones parameters for LiFSA using the GA-GPR active learning framework demonstrated efficient exploration of the parameter space and rapid convergence. Initially, the surrogate model was trained on 160 data points, with 40 reserved for testing. This foundation allowed the model to begin exploring the parameter space effectively. The iterative nature of the active learning process proved crucial in refining the model's predictive capabilities. After each iteration, the training data set was updated with new data points, and the model was retrained. This continuous refinement enabled the model to progressively adapt its understanding of the parameter landscape.

The genetic algorithm played a key role in generating diverse parameter sets. In each iteration, 500 new parameter combinations were created, from which 10−15 were selected based on the lowest fitness predicted by the GPR (eq 1). This approach ensured a balance between the exploration of new parameter regions and the exploitation of promising areas. As shown in Figure 2, the fitness evolution demonstrates a clear

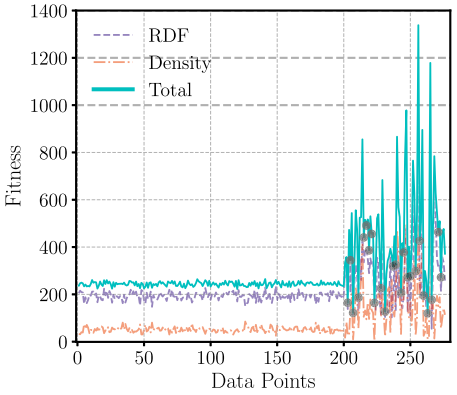

Figure 2. Evolution of fitness values during the GA-GPR optimization process for LiFSA force field parameters.

improvement trend over the training steps. The initial iterations show a widespread of fitness values, indicating the model's broad exploration of the parameter space. As the training progressed, the fitness values converged toward lower values, signifying the model's increasing ability to identify optimal parameter sets.

The optimization process reached convergence after 7 iterations, resulting in a final data set of 275 parameters. This relatively small number of iterations highlights the efficiency of the GA-GPR approach in navigating the complex parameter space of LiFSA. The final parameter set achieved optimal performance in reproducing both density and radial distribution functions, demonstrating the success of the optimization strategy in balancing multiple objectives. This efficient parametrization process underscores the power of combining genetic algorithms with Gaussian process regression in an active learning framework for force field optimization.

To assess the accuracy of the GA-GPR optimized force field, we compared its performance against the standard OPLS force field. The optimized LJ parameters and atomic site charges are summarized in Table 1. The bonded interaction parameters in the FSA anion are tabulated in Table S1. A key difference is the cationic charge of lithium, which was calculated as 0.925828e using the DDEC6 method, compared to the full +1e charge in OPLS. This charge modification, along with the revised nonbonded parameters, plays a crucial role in the accuracy of the force field.

The GA-GPR refined parameters demonstrate superior performance in reproducing both the density and structural properties of LiFSA. As shown in Table 2, the calculated density using GA-GPR parameters is 1803.28 kg m^{-3}, which deviates by only −4.47% from the AIMD reference. In contrast, the OPLS parameters overestimate the density by 9.75%. This overestimation by OPLS can be attributed to the stronger electrostatic interactions resulting from the higher partial charges, leading to a more compressed volume. In the absence of experimentally reported density data for liquid LiFSA, we used reference data from AIMD simulations

https://doi.org/10.1021/acs.jpcb.5c02097
J. Phys. Chem. B XXXX, XXX, XXX−XXX

Table 1. Optimized GA-GPR Force Field Parameters for LiFSA, Including Atom Names, Partial Charges, and Lennard-Jones Parameters (σ and ϵ), Shown Alongside Corresponding OPLS Parameters for Comparison

	GA-GPR			OPLS		
atoms	charges (e)	σ (nm)	ϵ (kJ/mol)	charges (e)	σ (nm)	ϵ (kJ/mol)
N	−1.019366	0.367716	0.728962	−0.42	0.3250	0.711
SF1	1.557158	0.290627	0.825059	1.02	0.3550	1.046
SF2	1.523893	0.290627	0.825059	1.02	0.3550	1.046
F1	−0.295356	0.365354	0.300636	−0.13	0.2950	0.222
F2	−0.268488	0.365354	0.300636	−0.13	0.2950	0.222
OF1	−0.571006	0.299736	0.807669	−0.59	0.2960	0.879
OF2	−0.584459	0.299736	0.807669	−0.59	0.2960	0.879
OF3	−0.532748	0.299736	0.807669	−0.59	0.2960	0.879
OF4	−0.735456	0.299736	0.807669	−0.59	0.2960	0.879
Li	0.925828	0.262330	0.001735	1.00	0.1582	1.409

Table 2. Comparison of Liquid Phase Density (kg m^{-3}) of LiFSA at 423 K Obtained from AIMD, GA-GPR Optimized Force Field, and OPLS Parameters

	AIMD	GA-GPR	% deviation	OPLS	% deviation
LiFSA	1887.6	1803.28 ± 1.30	−4.47	2071.55 ± 0.41	9.75

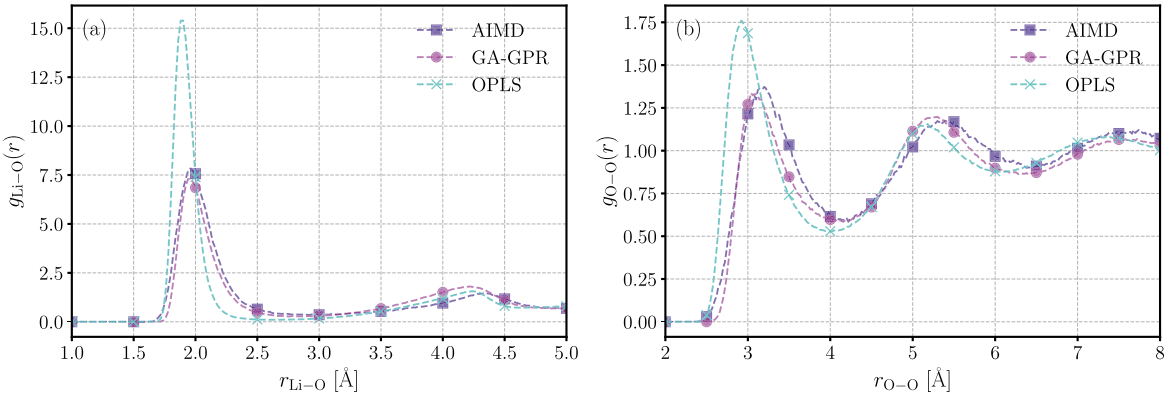

Figure 3. Comparison of radial distribution functions for (a) Li−O and (b) O−O atom pairs in LiFSA at 423 K. Results from AIMD (blue), GA-GPR optimized force field (magenta), and OPLS force field (cyan) are shown. The GA-GPR model demonstrates excellent agreement with AIMD reference data, while OPLS shows significant deviations.

performed at the PBE-D3 level. This choice is supported by previous studies where PBE-D3 reliably reproduced structural and thermophysical properties of similar ionic liquids.[15,58] We validated our AIMD setup to ensure reliability by confirming that the computed density aligns well with available experimental data reported for sulfones in the liquid phase and related electrolyte systems.[24] Therefore, AIMD-derived density and RDFs were used as consistent and physically meaningful targets for force field optimization.

Structural validation was performed by comparing the Li−O and O−O radial distribution functions calculated using GA-GPR, OPLS, and AIMD methods. As shown in Figure 3a, the Li−O RDF reveals that OPLS predicts a higher probability of oxygen atoms being closer to the lithium cation compared to both GA-GPR and AIMD results. This is consistent with the overestimated partial charges in OPLS. Notably, the GA-GPR refined force field shows excellent agreement with the AIMD Li−O distribution, accurately capturing the solvation structure around the lithium cation. The O−O RDF (Figure 3b) further confirms the improved accuracy of the GA-GPR model. It closely matches the AIMD reference, correctly representing the oxygen−oxygen correlations within the FSA anion and between different anions. The OPLS force field, however, shows significant deviations in peak positions and heights for both RDFs. Based on these structural validations and the improved density prediction, the GA-GPR refined force field was selected for subsequent mixture simulations.

3.2. LiFSA-Sulfone Binary Mixtures. After optimizing the force field parameters for pure LiFSA using the GA-GPR approach, we applied these parameters to simulate binary mixtures at 303 K. The simulation details are discussed in the Method section. This step is crucial in validating the transferability and accuracy of our developed force field, as the parametrization was performed on individual species rather than their mixtures. To evaluate the reliability of our simulations, we focused on both the structural and transport properties of the mixtures. We chose a 1:3 salt-to-solvent ratio based on experimental measurements, allowing for direct comparison between our simulations and experimental results.[4] The number of molecules was adjusted to maintain comparable atom counts across systems: LiFSA/SL (800:2400), LiFSA/MSL (700:2100), LiFSA/DMS (1000:3000), and LiFSA/EMS (800:2400). This approach ensures better statistical accuracy and reduces fluctuations in the dynamics across the four mixtures.

https://doi.org/10.1021/acs.jpcb.5c02097
J. Phys. Chem. B XXXX, XXX, XXX−XXX

Table 3. Comparison of Simulated and Experimental Densities[4] (kg m^{-3}) for 1:3 LiFSA-Sulfone Mixtures[a]

system	exp	GA-GPR	% deviation	OPLS	% deviation
LiFSA-SL	1458	1431.92 ± 0.53	−1.78	1530.08 ± 0.58	4.94
LiFSA-MSL	1375	1368.61 ± 0.82	−0.46	1426.57 ± 0.66	3.75
LiFSA-DMS	1474	1478.41 ± 0.31	0.30	1534.75 ± 0.57	4.12
LiFSA-EMS	1389	1405.11 ± 0.27	1.16	1454.72 ± 0.24	4.73

[a]Results are shown for both GA-GPR optimized force field and conventional OPLS force field. The percentage deviation from experimental values highlights the improved accuracy of the GA-GPR model over OPLS in reproducing liquid-phase density.

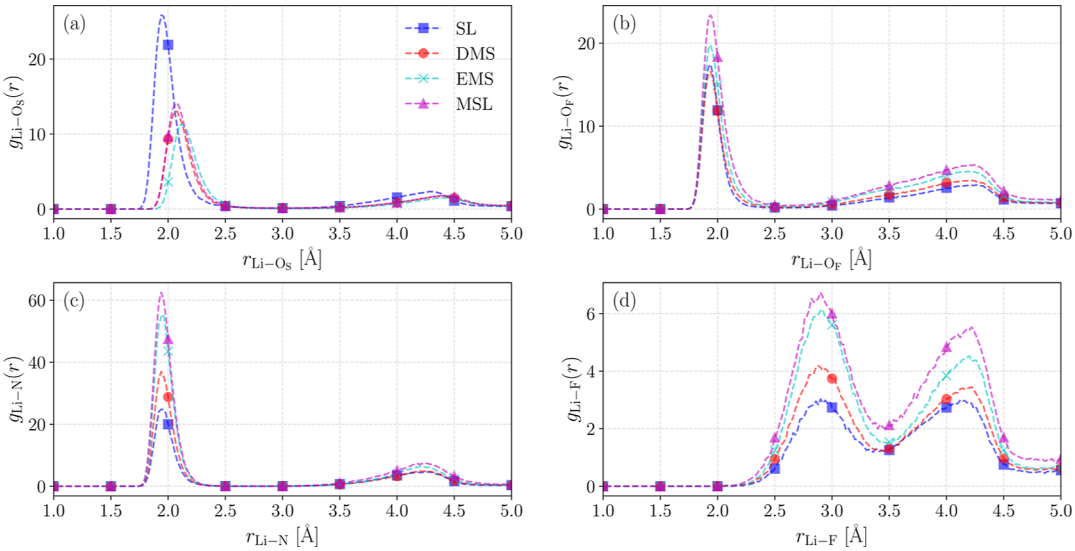

Figure 4. Radial distribution functions for lithium ion interactions in LiFSA-sulfone mixtures. (a) Li−O_S RDFs showing lithium coordination by solvent oxygen atoms. (b) Li−O_F, (c) Li−N, and (d) Li−F RDFs illustrate lithium interactions with the FSA anion's oxygen, nitrogen, and fluorine atoms, respectively.

The density comparison between simulations using the GA-GPR optimized force field and experimental values for 1:3 LiFSA-sulfone mixtures demonstrates excellent agreement across all systems studied, as summarized in Table 3. The density calculations were performed using the last 3 ns of the equilibrated trajectory and averaged over three 1 ns blocks. Our simulations accurately capture the density trends observed experimentally, with deviations ranging from −1.78% to 1.16%. The LiFSA-DMS shows the closest agreement, with a minor deviation of only 0.30%. Interestingly, the simulations slightly underestimate LiFSA-SL and LiFSA-MSL density while slightly overestimating it for LiFSA-DMS and LiFSA-EMS. A notable observation is the lower density of mixtures containing asymmetric sulfones (MSL, EMS) compared to those with symmetric sulfones (SL, DMS). This trend is consistent in both experimental and simulated results. The structural asymmetry of MSL and EMS likely introduces steric hindrance, limiting the proximity between ions and solvent molecules. In contrast, the symmetric nature of SL and DMS allows for more efficient packing and stronger interactions with the ionic species.

To benchmark the performance of our GA-GPR parameters, we also performed NPT simulations using the conventional OPLS force field and computed the corresponding mixture densities. As seen in Table 3, OPLS-based simulations systematically overestimate the densities across all systems, with deviations exceeding 3.7% in every case. This over-prediction indicates that OPLS parameters may lead to overstructured liquid phases, potentially arising from overly attractive nonbonded interactions or inadequate description of solvation structure around the ions. These inaccuracies can propagate into predicting other properties, especially transport coefficients. In contrast, the GA-GPR force field—optimized using a data-driven approach—exhibits significantly reduced error in reproducing experimental densities, thereby providing a more accurate description of ion−solvent interactions. This improvement underscores the advantage of physically informed machine learning techniques to refine classical force fields, particularly for complex ionic liquid systems. The better agreement with the experiment not only validates the transferability of the GA-GPR force field from pure components to binary mixtures but also establishes a reliable foundation for predictive simulations of structural and transport behavior in sulfone-based electrolytes.

3.2.1. Ion−Solvent Interactions. The solvation structure of lithium ions in different LiFSA-sulfone mixtures provides crucial insights into the molecular-level interactions that govern the electrolyte properties. Analysis of the radial distribution functions from the equilibrated MD trajectories reveals distinct coordination patterns around the lithium ions, as shown in Figure 4. The RDFs indicate that lithium cations interact closely with various atoms of the FSA anion. The Li−O_F (oxygen from FSA^-) and Li−N interactions exhibit prominent peaks just below 2 Å (Figure 4b,c), indicating strong coordination. In contrast, the Li−F interaction shows a peak near 3 Å, with a second peak visible within 4.5 Å (Figure 4d), suggesting two distinct fluorine environments in the first and second coordination shells. A key observation is the competitive coordination of lithium ions by oxygens from the solvent (O_S) and the FSA anion (O_F). While O_F generally

https://doi.org/10.1021/acs.jpcb.5c02097
J. Phys. Chem. B XXXX, XXX, XXX−XXX

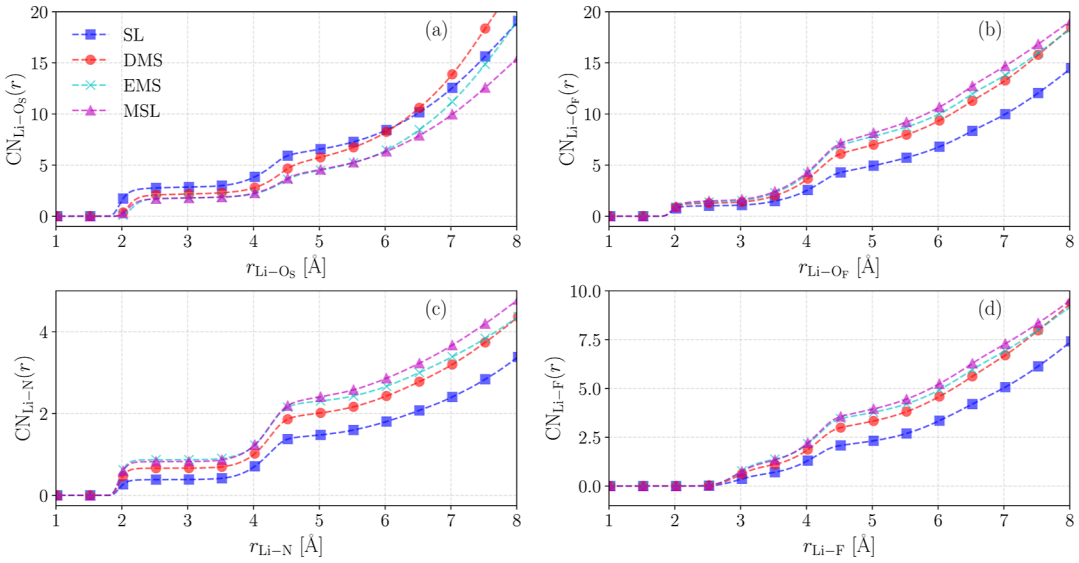

Figure 5. Coordination number profiles derived from the production run trajectory, showing Li^+ coordination with (a) solvent oxygen (O_S), (b) oxygen (O_F), (c) nitrogen (N), and (d) fluorine (F) atoms from FSA anion.

coordinate more closely to lithium, the solvent oxygen behavior varies among the different sulfones (Figure 4a). SL (sulfolane) shows the strongest O_S coordination to lithium among all solvents, with its peak nearly matching that of O_F. MSL (3-methylsulfolane) exhibits the highest O_F coordination probability, suggesting weaker solvent interaction. DMS and EMS show intermediate behavior, with O_S peaks slightly lower and further from lithium than O_F. The strongest Li−O_S coordination in the LiFSA-SL mixture can be attributed to the largest dipole moment observed in the pure SL, as reported in our previous study on pristine sulfone systems.[24]

The coordination strength of N and F atoms to lithium follows the trend: EMS ≃ MSL > DMS > SL. The coordination number plots are displayed in Figure 5. This trend correlates inversely with the solvent's ability to coordinate lithium, suggesting a competition between the solvent and the anion for lithium coordination. The strong O_S coordination in SL suggests better solvation of lithium ions, potentially creating a dielectric barrier between Li^+ and FSA^- ions. This weakens the strong electrostatic interactions, likely contributing to the lower viscosity observed for LiFSA-SL mixtures.[4] Conversely, the weaker O_S coordination in MSL allows for stronger Li−O_F interactions, explaining the higher viscosity observed in LiFSA-MSL mixtures. The strong ionic associations in this case may impede ion mobility. DMS and EMS show intermediate behavior, balancing solvent and anion coordination to lithium. This balance likely contributes to their moderate viscosity values compared to SL and MSL mixtures.[4] These solvation structure insights provide a molecular-level explanation for the macroscopic properties observed in the LiFSA-sulfone electrolyte mixtures, to be discussed in detail in the following sections, highlighting the crucial role of competitive coordination in determining electrolyte performance. Representative snapshots of the lithium ion's coordination environment in different binary mixtures, shown in Figure 6, further illustrate this trend. In the LiFSA-SL mixture, Li^+ is primarily coordinated by two oxygen atoms, each from SL molecules and the FSA anion. In contrast, in the other mixtures, the number of solvent oxygen atoms around Li^+ decreases relative to the FSA anion, consistent with the radial

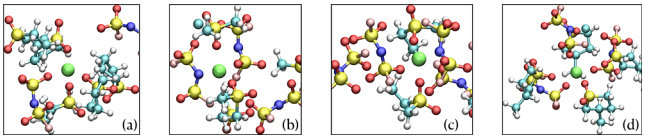

Figure 6. Representative coordination sphere around Li^+ in binary mixtures: (a) SL, (b) DMS, (c) EMS, and (d) MSL. Color scheme: Li—green; H—white; C—cyan; N—blue; O—red; and S—yellow.

distribution function trends observed in Figure 4. This structural variation reinforces the observed ion association and viscosity differences across the mixtures.

To deepen our understanding of the molecular interactions in LiFSA-sulfone mixtures, we analyzed the RDFs for Li−Li, Li−solvent, and FSA-solvent pairs, as shown in Figure 7. These RDFs reveal distinct coordination patterns shaped by the structural symmetry and molecular volume of the sulfone solvents. The Li−Li RDFs (Figure 7a) demonstrate significant variations in ion−ion associations across different solvents. MSL shows the strongest Li−Li interactions, indicated by the tallest peak at approximately 4 Å, reflecting the close proximity of lithium ions. EMS exhibits a similar trend but with an additional shoulder peak at around 5 Å, hinting at weaker secondary interactions beyond this distance. In contrast, SL and DMS display weaker Li−Li correlations, characterized by broader and lower-intensity peaks. This difference suggests that asymmetric sulfones (MSL and EMS) promote stronger ion−ion associations due to their reduced ability to effectively solvate lithium ions, unlike the symmetric sulfones (SL and DMS). Further insights are gained from the Li-solvent RDFs (Figure 7b), highlighting the impact of molecular volume on solvation behavior. With smaller molecular volumes, the aliphatic sulfones, DMS, and EMS facilitate interactions at shorter distances, allowing for closer lithium-solvent contact. In contrast, the larger cyclic sulfones, SL and MSL, coordinate lithium ions at slightly longer distances due to their bulkier structure. Additionally, the FSA-solvent RDFs shown in Figure 7c shed light on anion−solvent coordination. A small peak at approximately 4.25 Å is observed in all mixtures, indicating short-range solvent−anion interactions. Among the solvents,

https://doi.org/10.1021/acs.jpcb.5c02097
J. Phys. Chem. B XXXX, XXX, XXX−XXX

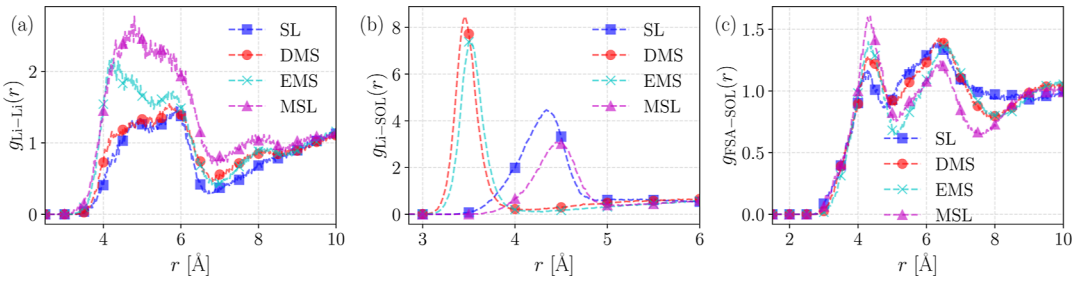

Figure 7. Radial distribution functions for various interactions in LiFSA-sulfone mixtures. (a) Li−Li correlations; (b) Li-Solvent RDFs depicting interactions between lithium ions and sulfone solvent molecules; (c) FSA-Solvent RDFs illustrating correlations between FSA anions and sulfone solvent molecules.

MSL exhibits a slightly higher peak intensity at this distance, reflecting enhanced solvent access to the FSA anions. Conversely, SL displays the lowest peak height, suggesting weaker solvent−anion interactions. These findings collectively highlight how variations in sulfone symmetry and molecular size influence ion association and solvation dynamics in LiFSA-based electrolyte mixtures.

The RDF analyses underscore the critical role of sulfone symmetry in shaping electrolyte interactions. Symmetric sulfones, such as SL and DMS, tend to enhance Li^+-solvent interactions while reducing ion−ion associations. In contrast, asymmetric sulfones, MSL, and EMS promote stronger ion−ion interactions but weaken Li^+-solvent coordination. These distinct interaction patterns at the molecular level offer valuable insights into the variations in macroscopic properties—such as viscosity and ionic conductivity—observed across the different LiFSA-sulfone mixtures.

The two-dimensional correlation plots between the distance (r) of lithium ions from the sulfone center of geometry and the angle (ϕ) formed by the sulfone's oxygen bisector axis provide valuable insights into solvation dynamics across the four LiFSA-sulfone binary mixtures. Figure 8a illustrates the vectors used to define the angle between the Li^+ ion and the sulfone molecular axis. These plots highlight how sulfone symmetry and structure influence Li^+ coordination. For SL (Figure 9a),

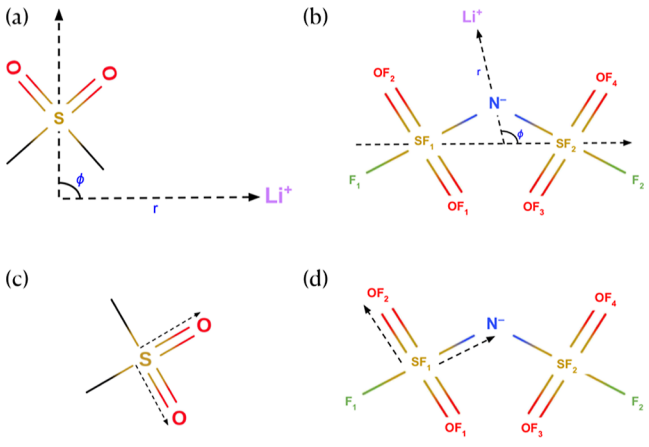

Figure 8. Schematic illustration of the vectors used to define angular orientations in the analysis for the angular distribution analysis between Li^+ and the sulfone (a) and FSA anion (b). For the rotational autocorrelation function analysis, the orientation vector for sulfone molecules is defined using the S−O−O triplet (c), and for the FSA anion, the rotational vector is defined using the SF−N−OF atom triplet (d).

the distribution peaks at $r \approx 4.25$ Å and spans a broad angular range ($\phi \approx 120°-150°$), reflecting its symmetric structure that allows flexible bridging coordination between Li^+ and sulfonyl oxygens. This distribution suggests a dynamic solvation shell and a coordination environment consistent with the relatively weak Li−Li correlations observed in the RDF analysis, where strong cation−solvent interactions dominate over ion−ion associations. DMS and EMS (Figure 9b,c) exhibit similar angular distributions but differ slightly in their distance peaks. DMS has a sharper peak at $r \approx 3.5$ Å, while EMS shows a slightly shifted peak near $r \approx 3.7$ Å. This closer Li^+ coordination, combined with the narrower angular range ($\phi \approx 100°-130°$), reflects compact monodentate interactions that align with the moderate Li−Li RDF peaks. The similarity in their angular patterns suggests comparable solvation behavior, although EMS's slightly larger distribution radius hints at subtle differences in solvation strength. In contrast, MSL (Figure 9d) displays a shifted peak at $r \approx 4.5$ Å and a broader angular range ($\phi \approx 130°-150°$), indicating weaker and more distant Li^+-sulfone coordination due to its bulkier asymmetric structure. This reduced solvation strength aligns with the stronger Li−Li correlations observed in the RDF analysis for MSL, where ionic aggregation dominates due to weaker cation−solvent interactions. The longer coordination distance and broader angular range reflect solvation characteristics typically associated with systems prone to ionic clustering.

To further probe ion-pairing behavior, we extended a similar analysis to explore the FSA anion's arrangement around Li^+ (see Figure 8b for angle definition). Figure S2 presents two-dimensional correlation plots with the distance (r) between Li^+ and the center of geometry of the FSA anion on the x-axis and the angle (ϕ) formed between two axes—one connecting Li^+ to the nitrogen atom in FSA and the other passing through the two sulfur atoms—on the y-axis. Although the overall distribution patterns are similar across all mixtures, variations in relative density suggest differences in the degree of Li^+ solvation by FSA anions. These subtle variations reflect the competitive coordination dynamics between sulfone solvents and FSA anions, as previously indicated by the RDF analyses. Together, these findings provide a molecular-level perspective on the solvation environment in LiFSA-sulfone mixtures and its influence on the observed macroscopic electrolyte properties.

3.2.2. Rotational Autocorrelation Functions. To gain deeper insights into the dynamic behavior of solvents and FSA anions in LiFSA-sulfone binary mixtures, we analyzed the rotational autocorrelation functions, which describe how molecular rotation evolves over time and influence ion transport. The RACF slopes indicate how quickly a molecule

https://doi.org/10.1021/acs.jpcb.5c02097
J. Phys. Chem. B XXXX, XXX, XXX−XXX

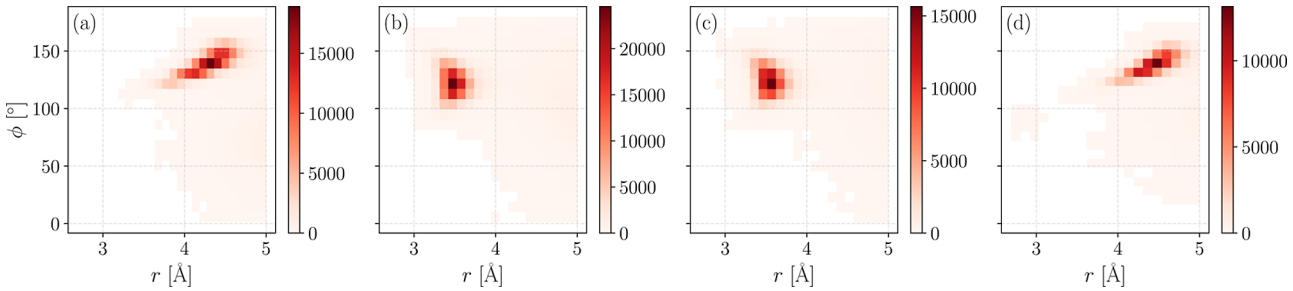

Figure 9. Two-dimensional correlation plots showing the relationship between the distance (r) from the Li^+ cation to the sulfone molecule's center of geometry and the angle (ϕ) between the Li^+-sulfone axis and the axis bisecting the sulfone's oxygen atoms. Panels (a) SL, (b) DMS, (c) EMS, and (d) MSL illustrate how molecular symmetry influences Li^+ coordination and solvation dynamics. The intensity of the color represents the density of configurations, providing insights into the spatial arrangement of sulfone molecules around Li^+ ions.

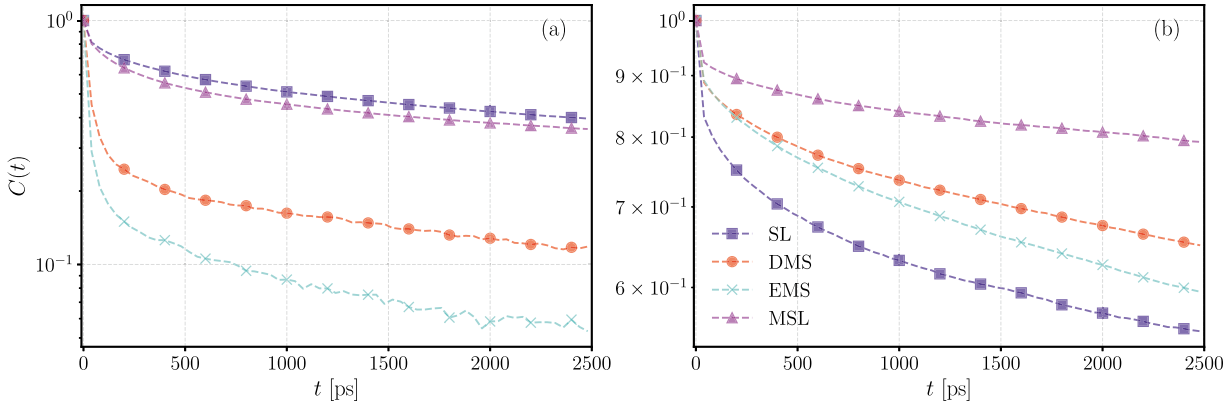

Figure 10. Rotational autocorrelation function, $C(t)$, as a function of time (t) for binary mixtures of four solvents (SL, DMS, EMS, and MSL) with LiFSA: (a) solvent dynamics and (b) anion dynamics.

Table 4. Comparison of Viscosity and Conductivity Obtained from Classical MD Simulations Employing GA-GPR Force Fields, with Experimental Measurements[4]

mixtures	viscosity (cP)			conductivity (mS cm^{-1})		
	exp	GA-GPR	Δ %	exp	GA-GPR	Δ %
LiFSA-SL	121	123.51 ± 1.63	2.02	2.19	2.18 ± 0.14	−0.46
LiFSA-MSL	148	139.85 ± 1.18	−5.50	1.35	1.45 ± 0.08	7.40
LiFSA-DMS	119	124.77 ± 1.45	4.85	2.40	2.42 ± 0.06	0.83
LiFSA-EMS	122	124.80 ± 0.97	2.29	1.65	1.70 ± 0.10	3.03

loses memory of its initial orientation, with steeper slopes corresponding to faster rotational dynamics. The rotational autocorrelation function was computed by defining a vector normal to a molecular plane formed by a triplet of atoms. For sulfones, the (S−O−O) triplet was used to define the orientation vector of the SO_2 group. The vector was defined using the SF−N−OF triplet for the FSA anion to represent the core orientation. These selections effectively capture the relevant rotational dynamics of the solute species. Figure 8c,d provide illustrative diagrams showing the chosen vectors. Figure 10a presents the RACFs of the sulfone solvents, highlighting distinct trends based on molecular structure and symmetry. Aliphatic sulfones (DMS and EMS) exhibit faster rotational decay than their cyclic counterparts (SL and MSL), as reflected by the steeper RACF slopes. This faster rotation is attributed to their smaller molecular volumes and the absence of rigid cyclic ring geometry, which minimizes rotational resistance. Within each structural class, the asymmetric sulfones (MSL and EMS) display even faster rotational decay than the symmetric ones (SL and DMS). This behavior arises from the asymmetry-induced shift in their center of mass, which reduces their moment of inertia and facilitates faster rotation.

Figure 10b shows the RACFs of the FSA anions in the different sulfone mixtures, providing further insights into anion dynamics. The rotational decay of FSA^- is fastest in the LiFSA-SL mixture and slowest in the LiFSA-MSL mixture, with DMS and EMS mixtures showing intermediate and nearly identical behavior. This trend aligns with the anion−solvent interactions observed in the FSA-solvent RDFs. Specifically, MSL exhibited the tallest first RDF peak in Figure 7c, indicating strong and localized interactions that restrict FSA's rotational freedom, while SL displayed the weakest peak, consistent with the faster anionic rotation observed in its RACF. Overall, the RACF analyses reveal that both solvent structure and solvent−anion interactions significantly impact rotational dynamics, which in turn influence the microscopic environment governing ion transport. These findings complement earlier RDF observations, providing a dynamic perspective on how molecular

https://doi.org/10.1021/acs.jpcb.5c02097
J. Phys. Chem. B XXXX, XXX, XXX−XXX

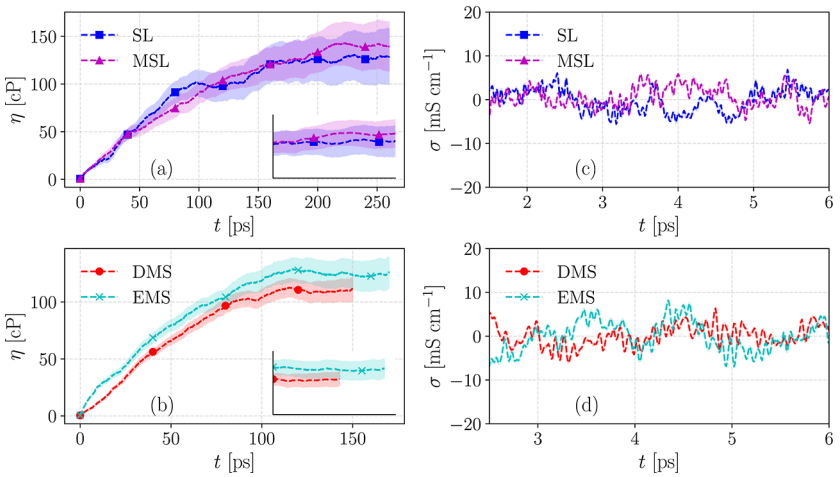

Figure 11. (a,b) Viscosity (η) and (c,d) ionic conductivity (σ) computed using the Green−Kubo formalism (eqs 5 and 6) as a function of correlation time for LiFSA-sulfone mixtures. The shaded regions represent the uncertainty in the calculated values for each mixture. The insets show the converged part of the running integral.

structure affects the solvation environment and coordination dynamics in LiFSA-sulfone electrolytes.

3.2.3. Transport Properties. The transport properties of LiFSA-sulfone mixtures, specifically viscosity and conductivity, were evaluated using the Green−Kubo formalism (eqs 5 and 6), which integrates the pressure tensor and electric current autocorrelation functions, respectively. The computed values, summarized in Table 4, exhibit excellent agreement with experimental data, with deviations within 7.5%, validating the reliability of the GA-GPR optimized force fields. This agreement highlights the effectiveness of the parametrization workflow, which accurately captures nonbonded interactions in pure systems and seamlessly extends these parameters to mixtures without additional optimization.

Viscosity calculations, yielded average values derived from the converged portion of the correlation time (Figure 11a,b). The simulated viscosities closely align with experimental values, with deviations ranging from 4.85% (LiFSA-DMS) to −5.50% (LiFSA-MSL). For instance, MSL, with the highest experimental viscosity (148 cP), shows a simulated value of 139.85 cP, corresponding to a deviation of −5.50%. Notably, binary mixtures containing symmetric sulfones (SL and DMS) exhibit lower viscosities compared to those with asymmetric sulfones (MSL and EMS). This can be attributed to the differences in ion−solvent interactions and resultant variations in molecular packing and solvation dynamics, as discussed earlier.

Conductivity, another essential transport property, was also computed using the Green−Kubo formalism (eq 6). The results, plotted in Figure 11c,d, reveal a maximum deviation of 7.40% for LiFSA-MSL, where the experimental conductivity of 1.35 mS cm^{-1} corresponds to a simulated value of 1.45 mS cm^{-1}. The closest match occurs in the LiFSA-SL mixture, with a simulated conductivity of 2.18 mS cm^{-1} closely reflecting the experimental value of 2.19 mS cm^{-1} (−0.46% deviation). The observed conductivity trend—DMS > SL > EMS > MSL—is consistent between simulations and experiments. This trend, as shown in Table 4, indicates that mixtures with symmetric sulfones (SL and DMS) generally exhibit higher conductivities than their asymmetric counterparts (EMS and MSL), likely due to the enhanced symmetry-driven solvation and ion transport dynamics. Interestingly, while conductivity varies notably across mixtures, viscosities for SL, DMS, and EMS are relatively similar despite their structural differences. This indicates that conductivity is more sensitive to collective atomic behavior and ion−solvent interactions than viscosity. The overall agreement between simulated and experimental transport properties confirms the robustness of the GA-GPR optimized force fields in describing both structural and dynamic characteristics of LiFSA-sulfone mixtures. These findings underscore the versatility of the parametrization workflow, which successfully delivers transferable force fields capable of accurately capturing the intricate electrolyte behavior at both microscopic and macroscopic scales.

To further assess the quality of our GA-GPR force field, we computed the self-diffusion coefficients of Li^+ and FSA^- ions using mean-squared displacement analysis from the MD trajectories. Table 5 shows that the computed diffusion

Table 5. Comparison of Diffusion Coefficients (10^{-7} cm^2/s) for Lithium (D_{Li^+}) and FSA Anion (D_{FSA^-}) Obtained from Classical MD Simulations Employing GA-GPR Force Fields, with Experimental Measurements[4]

mixtures	D_{Li^+}		D_{FSA^-}		D_{Li^+}/D_{FSA^-}	
	exp	GA-GPR	exp	GA-GPR	exp	GA-GPR
LiFSA-SL	1.63	0.16	1.29	0.13	1.26	1.18
LiFSA-MSL	1.08	0.13	1.07	0.17	1.01	0.80
LiFSA-DMS	1.63	0.18	1.84	0.19	0.89	0.98
LiFSA-EMS	1.05	0.52	1.29	0.54	0.81	0.96

coefficients are systematically lower than the experimental values, a known limitation of classical MD simulations due to overestimated solvent viscosities. Nevertheless, the ratio of D_{Li^+} to D_{FSA^-} is well preserved across all solvent systems, indicating that the force field accurately captures the relative ion mobilities. This consistency is particularly encouraging in light of recent findings that force field optimization often leads to an imbalance between ionic conductivity and diffusivity.[59] Our results suggest that the GA-GPR approach yields a more balanced and transferable description of ion transport in sulfone-based electrolytes.

We calculated the ratios of different relative coordination numbers to explore the relationship between transport

https://doi.org/10.1021/acs.jpcb.5c02097
J. Phys. Chem. B XXXX, XXX, XXX−XXX

properties and local solvation environments, as shown in Figure 12. The heatmap reveals a clear trend: relative

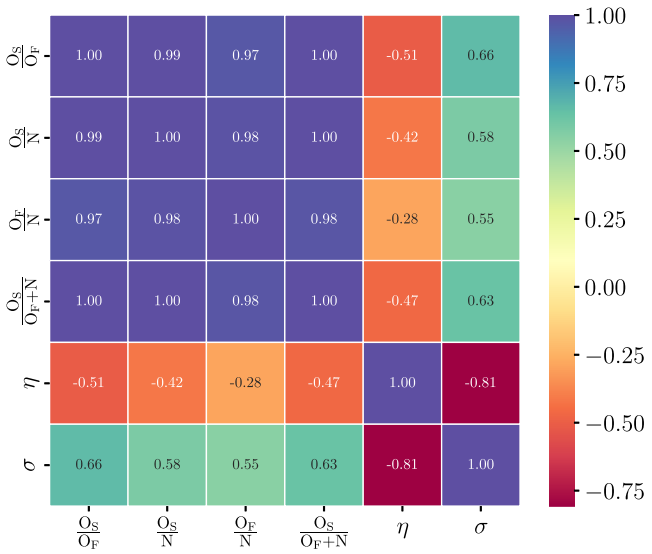

Figure 12. Heatmap depicting the correlation between transport properties (viscosity, η, and conductivity, σ) and relative coordination number ratios ($\frac{O_S}{O_F}$, $\frac{O_S}{N}$, $\frac{O_F}{N}$, and $\frac{O_S}{O_F+N}$) in LiFSA-sulfone mixtures. The negative correlation with viscosity and positive correlation with conductivity highlight the significant influence of solvent oxygen (O_S) coordination on ion transport.

coordination numbers exhibit a negative correlation with viscosity and a positive correlation with conductivity. Among the various coordination number ratios, the $\frac{O_S}{O_F}$ ratio has the most significant impact on both transport properties, indicating that a higher proportion of solvent oxygen (O_S) relative to anion oxygen (O_F) reduces viscosity while enhancing conductivity. This aligns with our earlier observations from the RDF plots in Figure 4a,b, which demonstrated enhanced cation−solvent interactions in sulfolane (SL) mixtures. Additionally, the $\frac{O_S}{O_F+N}$ ratio also plays a crucial role, reflecting the combined effect of solvent oxygen and the oxygen and nitrogen atoms from the anion. This collective coordination highlights the interplay between ion solvation and molecular packing, directly influencing viscosity and conductivity trends. Specifically, higher coordination involving anionic atoms tends to increase viscosity, while enhanced coordination of O_S promotes higher conductivity by facilitating ion mobility.

These findings suggest that the relative coordination numbers can be tuned by altering the molar ratios of sulfones and lithium salt, thereby modulating the transport properties. This insight provides a microscopic understanding of how solvation structure and coordination influence macroscopic transport behavior in LiFSA-sulfone mixtures, offering potential strategies for optimizing electrolyte performance.

4. CONCLUSIONS

This study presents a robust and efficient framework for systematically developing accurate and transferable force fields for LiFSA-sulfone mixtures, leveraging a genetic algorithm and Gaussian process regression. The optimized force fields achieve remarkable agreement with experimental transport properties, including viscosity and ionic conductivity, with deviations within 7.5%. This high accuracy demonstrates the effectiveness of the GA-GPR workflow in capturing nonbonded interactions and extending these optimized parameters to mixed systems without additional refinement, thus enhancing the predictive power for complex electrolyte behavior.

The calculated viscosity and conductivity trends, derived using the Green−Kubo formalism, reflect the critical role of molecular symmetry, ion−solvent interactions, and solvation dynamics. Binary electrolyte mixtures with symmetric sulfones (SL and DMS) exhibit lower viscosities and higher conductivities than their asymmetric counterparts (EMS and MSL) due to enhanced ion mobility. These findings emphasize the delicate balance between solvent structure and ion transport in determining macroscopic properties. Furthermore, the heatmap analysis reveals strong correlations between relative coordination numbers and transport properties, particularly highlighting the dominant role of solvent oxygen (O_S) coordination in reducing viscosity and enhancing ionic conductivity. This analysis provides microscopic insights into the solvation shell structure and its direct impact on transport efficiency.

By linking solvation structure to macroscopic transport behavior, this study not only deepens our understanding of ion transport mechanisms in LiFSA-sulfone mixtures but also offers practical guidance for electrolyte design. The demonstrated versatility of the GA-GPR optimization strategy paves the way for the rational design of next-generation electrolytes with tunable properties tailored to meet the performance demands of future energy storage and conversion applications.

■ ASSOCIATED CONTENT

Data Availability Statement

Codes used to perform the GA-GPR training, relevant simulations, and all generated parameter sets are available at https://github.com/cocokane/LJ_paramopt_framework. Force field parameters are presented in the main text and the Supporting Information.

Supporting Information

The Supporting Information is available free of charge at https://pubs.acs.org/doi/10.1021/acs.jpcb.5c02097.

The Supporting Information contains a force field optimization workflow, two-dimensional correlations, and a table summarizing bonded interaction parameters in the FSA anion (PDF)

■ AUTHOR INFORMATION

Corresponding Author

Anirban Mondal − *Department of Chemistry, Indian Institute of Technology Gandhinagar, Gandhinagar, Gujarat 382355, India*; orcid.org/0000-0003-3029-8840; Email: amondal@iitgn.ac.in

Author

Yati − *Department of Chemistry, Indian Institute of Technology Gandhinagar, Gandhinagar, Gujarat 382355, India*

Complete contact information is available at: https://pubs.acs.org/10.1021/acs.jpcb.5c02097

Author Contributions

AM conceived the problem. Yati conducted all the simulations. Yati and AM analyzed the results and prepared the draft.

https://doi.org/10.1021/acs.jpcb.5c02097
J. Phys. Chem. B XXXX, XXX, XXX−XXX

Notes

The authors declare no competing financial interest.

■ ACKNOWLEDGMENTS

The authors gratefully acknowledge the Indian Institute of Technology Gandhinagar, India, for providing research facilities and financial support. We thank PARAM Ananta for computational resources.

■ REFERENCES

(1) Chu, S.; Cui, Y.; Liu, N. The path towards sustainable energy. *Nat. Mater.* **2017**, *16*, 16−22.
(2) Yamada, Y.; Wang, J.; Ko, S.; Watanabe, E.; Yamada, A. Advances and issues in developing salt-concentrated battery electrolytes. *Nat. Energy* **2019**, *4*, 269−280.
(3) Hossain, M. J.; Wu, Q.; Marin Bernardez, E. J.; Quilty, C. D.; Marschilok, A. C.; Takeuchi, E. S.; Bock, D. C.; Takeuchi, K. J.; Qi, Y. The relationship between ionic conductivity and solvation structures of localized high-concentration fluorinated electrolytes for lithium-ion batteries. *J. Phys. Chem. Lett.* **2023**, *14*, 7718−7731.
(4) Ugata, Y.; Chen, Y.; Sasagawa, S.; Ueno, K.; Watanabe, M.; Mita, H.; Shimura, J.; Nagamine, M.; Dokko, K. Eutectic electrolytes composed of $LiN(SO_2F)_2$ and sulfones for Li-ion batteries. *J. Phys. Chem. C* **2022**, *126*, 10024−10034.
(5) Furui, R.; Hayamizu, K.; Takahashi, K.; Tsuzuki, S.; Miyauchi, H.; Inaba, K.; Kawana, Y.; Umebayashi, Y.; Seki, S. Elucidation of Liquid Structures and Transport Properties of Highly Concentrated $LiN(SO_2F)_2$/Ethylene Carbonate Electrolytes. *J. Phys. Chem. C* **2023**, *127*, 10748−10756.
(6) Tong, J.; Wu, S.; Von Solms, N.; Liang, X.; Huo, F.; Zhou, Q.; He, H.; Zhang, S. The effect of concentration of lithium salt on the structural and transport properties of ionic liquid-based electrolytes. *Front. Chem.* **2020**, *7*, 945.
(7) Uchida, S.; Kiyobayashi, T. How does the solvent composition influence the transport properties of electrolyte solutions? $LiPF_6$ and LiFSA in EC and DMC binary solvent. *Phys. Chem. Chem. Phys.* **2021**, *23*, 10875−10887.
(8) Ugata, Y.; Chen, Y.; Miyazaki, S.; Sasagawa, S.; Ueno, K.; Watanabe, M.; Dokko, K. High-concentration $LiPF_6$/sulfone electrolytes: structure, transport properties, and battery application. *Phys. Chem. Chem. Phys.* **2023**, *25*, 29566−29575.
(9) Ikeda, S.; Tsuzuki, S.; Sudoh, T.; Shigenobu, K.; Ueno, K.; Dokko, K.; Watanabe, M.; Shinoda, W. Lithium-ion dynamics in sulfolane-based highly concentrated electrolytes. *J. Phys. Chem. C* **2023**, *127*, 13837−13845.
(10) Ugata, Y.; Hasegawa, G.; Kuwata, N.; Ueno, K.; Watanabe, M.; Dokko, K. Temperature dependency of ion transport in highly concentrated Li salt/sulfolane electrolyte solutions. *J. Phys. Chem. C* **2022**, *126*, 19084−19090.
(11) Watanabe, Y.; Ugata, Y.; Ueno, K.; Watanabe, M.; Dokko, K. Does Li-ion transport occur rapidly in localized high-concentration electrolytes? *Phys. Chem. Chem. Phys.* **2023**, *25*, 3092−3099.
(12) Hofmann, A.; Migeot, M.; Thißen, E.; Schulz, M.; Heinzmann, R.; Indris, S.; Bergfeldt, T.; Lei, B.; Ziebert, C.; Hanemann, T. Electrolyte Mixtures Based on Ethylene Carbonate and Dimethyl Sulfone for Li-Ion Batteries with Improved Safety Characteristics. *ChemSusChem* **2015**, *8*, 1892−1900.
(13) Das, A.; Riyaz, M.; Kobi, S.; Saha, D.; Mukhopadhyay, A. Ethylene Carbonate Free Sulfone-Based Electrolyte for Enabling Superior Performance of High Ni-containing Li-Transition Metal Oxide Cathodes at High Voltage and High Temperature. *Batter. Supercaps* **2025**, *8*, No. e202400608.
(14) Yang, Q.; Lv, X.; Fu, Y.; Xu, K.; Guo, W. Ligand exchange of Li-ion solvation sheath enables balanced electrolytes. *Joule* **2025**, *9*, 101821.
(15) Mukherji, S.; Avula, N. V.; Balasubramanian, S. Refined force field for liquid sulfolane with particular emphasis to its transport characteristics. *ACS Omega* **2020**, *5*, 28285−28295.
(16) Zhang, H.; Zou, J.; Shen, Z.; Liu, Z.; Hu, L.; Yue, H.; Chen, H.; Wu, Y.; Huang, S.; Li, Z.; et al. Sulfone additive enhanced ultrahigh energy density Li/CFx primary batteries. *J. Power Sources* **2025**, *630*, 236098.
(17) Yao, N.; Chen, X.; Fu, Z.-H.; Zhang, Q. Applying classical, ab initio, and machine-learning molecular dynamics simulations to the liquid electrolyte for rechargeable batteries. *Chem. Rev.* **2022**, *122*, 10970−11021.
(18) Mondal, A.; Balasubramanian, S. A molecular dynamics study of collective transport properties of imidazolium-based room-temperature ionic liquids. *J. Chem. Eng. Data* **2014**, *59*, 3061−3068.
(19) Tsuzuki, S.; Shinoda, W.; Matsugami, M.; Umebayashi, Y.; Ueno, K.; Mandai, T.; Seki, S.; Dokko, K.; Watanabe, M. Structures of $[Li(glyme)]^+$ complexes and their interactions with anions in equimolar mixtures of glymes and Li [TFSA]: analysis by molecular dynamics simulations. *Phys. Chem. Chem. Phys.* **2015**, *17*, 126−129.
(20) Gao, Y.; He, J.; Kang, J.; Peng, J.; Bian, H. Molecular Insights into Anion-Specific Freezing Point Depression in Lithium Salt Solutions. *J. Phys. Chem. B* **2025**, *129*, 2730−2738.
(21) Jorgensen, W. L.; Tirado-Rives, J. The OPLS [optimized potentials for liquid simulations] potential functions for proteins, energy minimizations for crystals of cyclic peptides and crambin. *J. Am. Chem. Soc.* **1988**, *110*, 1657−1666.
(22) Jorgensen, W. L.; Maxwell, D. S.; Tirado-Rives, J. Development and testing of the OPLS all-atom force field on conformational energetics and properties of organic liquids. *J. Am. Chem. Soc.* **1996**, *118*, 11225−11236.
(23) Dokko, K.; Watanabe, D.; Ugata, Y.; Thomas, M. L.; Tsuzuki, S.; Shinoda, W.; Hashimoto, K.; Ueno, K.; Umebayashi, Y.; Watanabe, M. Direct evidence for Li ion hopping conduction in highly concentrated sulfolane-based liquid electrolytes. *J. Phys. Chem. B* **2018**, *122*, 10736−10745.
(24) Yati; Kokane, Y.; Mondal, A. Active-Learning Assisted General Framework for Efficient Parameterization of Force-Fields. *J. Chem. Theory Comput.* **2025**, *21*, 2638−2654.
(25) Canongia Lopes, J. N.; Shimizu, K.; Pádua, A. A.; Umebayashi, Y.; Fukuda, S.; Fujii, K.; Ishiguro, S.-i. Potential energy landscape of bis (fluorosulfonyl) amide. *J. Phys. Chem. B* **2008**, *112*, 9449−9455.
(26) Mondal, A.; Balasubramanian, S. Quantitative prediction of physical properties of imidazolium based room temperature ionic liquids through determination of condensed phase site charges: A refined force field. *J. Phys. Chem. B* **2014**, *118*, 3409−3422.
(27) Mondal, A.; Balasubramanian, S. A refined all-atom potential for imidazolium-based room temperature ionic liquids: acetate, dicyanamide, and thiocyanate anions. *J. Phys. Chem. B* **2015**, *119*, 11041−11051.
(28) Wang, N.; Carlozo, M. N.; Marin-Rimoldi, E.; Befort, B. J.; Dowling, A. W.; Maginn, E. J. Machine learning-enabled development of accurate force fields for refrigerants. *J. Chem. Theory Comput.* **2023**, *19*, 4546−4558.
(29) Mondal, A.; Young, J. M.; Barckholtz, T. A.; Kiss, G.; Koziol, L.; Panagiotopoulos, A. Z. Genetic algorithm driven force field parameterization for molten alkali-metal carbonate and hydroxide salts. *J. Chem. Theory Comput.* **2020**, *16*, 5736−5746.
(30) Madin, O. C.; Shirts, M. R. Using physical property surrogate models to perform accelerated multi-fidelity optimization of force field parameters. *Digit. Discovery* **2023**, *2*, 828−847.
(31) Befort, B. J.; DeFever, R. S.; Tow, G. M.; Dowling, A. W.; Maginn, E. J. Machine learning directed optimization of classical molecular modeling force fields. *J. Chem. Inf. Model.* **2021**, *61*, 4400−4414.
(32) Boothroyd, S.; Wang, L.-P.; Mobley, D. L.; Chodera, J. D.; Shirts, M. R. Open force field evaluator: An automated, efficient, and scalable framework for the estimation of physical properties from molecular simulation. *J. Chem. Theory Comput.* **2022**, *18*, 3566−3576.
(33) Ringrose, C.; Horton, J. T.; Wang, L.-P.; Cole, D. J. Exploration and validation of force field design protocols through QM-to-MM mapping. *Phys. Chem. Chem. Phys.* **2022**, *24*, 17014−17027.

https://doi.org/10.1021/acs.jpcb.5c02097
J. Phys. Chem. B XXXX, XXX, XXX−XXX

(34) Kantonen, S. M.; Muddana, H. S.; Schauperl, M.; Henriksen, N. M.; Wang, L.-P.; Gilson, M. K. Data-driven mapping of gas-phase quantum calculations to general force field Lennard-Jones parameters. *J. Chem. Theory Comput.* **2020**, *16*, 1115−1127.
(35) Limas, N. G.; Manz, T. A. Introducing DDEC6 atomic population analysis: part 4. Efficient parallel computation of net atomic charges, atomic spin moments, bond orders, and more. *RSC Adv.* **2018**, *8*, 2678−2707.
(36) Manz, T. A. Introducing DDEC6 atomic population analysis: part 3. Comprehensive method to compute bond orders. *RSC Adv.* **2017**, *7*, 45552−45581.
(37) Frisch, M. J.; Trucks, G. W.; Schlegel, H. B.; Scuseria, G. E.; Robb, M. A.; Cheeseman, J. R.; Scalmani, G.; Barone, V.; Mennucci, B.; Petersson, G. A.; et al. *Gaussian 09*. Revision E.01; Gaussian Inc.: Wallingford CT, 2009.
(38) Martínez, L.; Andrade, R.; Birgin, E. G.; Martínez, J. M. PACKMOL: A package for building initial configurations for molecular dynamics simulations. *J. Comput. Chem.* **2009**, *30*, 2157−2164.
(39) Pronk, S.; Páll, S.; Schulz, R.; Larsson, P.; Bjelkmar, P.; Apostolov, R.; Shirts, M. R.; Smith, J. C.; Kasson, P. M.; Van Der Spoel, D.; et al. GROMACS 4.5: a high-throughput and highly parallel open source molecular simulation toolkit. *Bioinformatics* **2013**, *29*, 845−854.
(40) Hess, B.; Kutzner, C.; Van Der Spoel, D.; Lindahl, E. GROMACS 4: algorithms for highly efficient, load-balanced, and scalable molecular simulation. *J. Chem. Theory Comput.* **2008**, *4*, 435−447.
(41) Bussi, G.; Donadio, D.; Parrinello, M. Canonical sampling through velocity rescaling. *J. Chem. Phys.* **2007**, *126*, 014101.
(42) Berendsen, H. J.; Postma, J. v.; Van Gunsteren, W. F.; DiNola, A.; Haak, J. R. Molecular dynamics with coupling to an external bath. *J. Chem. Phys.* **1984**, *81*, 3684−3690.
(43) Darden, T.; York, D.; Pedersen, L. Particle mesh Ewald: An N log (N) method for Ewald sums in large systems. *J. Chem. Phys.* **1993**, *98*, 10089.
(44) Kühne, T. D.; Iannuzzi, M.; Del Ben, M.; Rybkin, V. V.; Seewald, P.; Stein, F.; Laino, T.; Khaliullin, R. Z.; Schütt, O.; Schiffmann, F.; et al. CP2K: An electronic structure and molecular dynamics software package-Quickstep: Efficient and accurate electronic structure calculations. *J. Chem. Phys.* **2020**, *152*, 194103.
(45) VandeVondele, J.; Krack, M.; Mohamed, F.; Parrinello, M.; Chassaing, T.; Hutter, J. Quickstep: Fast and accurate density functional calculations using a mixed Gaussian and plane waves approach. *Comput. Phys. Commun.* **2005**, *167*, 103−128.
(46) Hutter, J.; Iannuzzi, M.; Schiffmann, F.; VandeVondele, J. cp2k: atomistic simulations of condensed matter systems. *Wiley Interdiscip. Rev.: Comput. Mol. Sci.* **2014**, *4*, 15−25.
(47) Perdew, J. P.; Burke, K.; Ernzerhof, M. Generalized gradient approximation made simple. *Phys. Rev. Lett.* **1996**, *77*, 3865.
(48) Grimme, S.; Antony, J.; Ehrlich, S.; Krieg, H. A consistent and accurate ab initio parametrization of density functional dispersion correction (DFT-D) for the 94 elements H-Pu. *J. Chem. Phys.* **2010**, *132*, 154104.
(49) Goedecker, S.; Teter, M.; Hutter, J. Separable dual-space Gaussian pseudopotentials. *Phys. Rev. B* **1996**, *54*, 1703.
(50) Hartwigsen, C.; Gœdecker, S.; Hutter, J. Relativistic separable dual-space Gaussian pseudopotentials from H to Rn. *Phys. Rev. B* **1998**, *58*, 3641.
(51) Martyna, G. J.; Tobias, D. J.; Klein, M. L. Constant pressure molecular dynamics algorithms. *J. Chem. Phys.* **1994**, *101*, 4177−4189.
(52) Martyna, G. J.; Klein, M. L.; Tuckerman, M. Nosé−Hoover chains: The canonical ensemble via continuous dynamics. *J. Chem. Phys.* **1992**, *97*, 2635−2643.
(53) Pedregosa, F.; Varoquaux, G.; Gramfort, A.; Michel, V.; Thirion, B.; Grisel, O.; Blondel, M.; Prettenhofer, P.; Weiss, R.; Dubourg, V.; et al. Scikit-learn: Machine learning in Python. *J. Mach. Learn. Res.* **2011**, *12*, 2825−2830.
(54) Fortin, F.-A.; De Rainville, F.-M.; Gardner, M.-A. G.; Parizeau, M.; Gagné, C. DEAP: Evolutionary algorithms made easy. *J. Mach. Learn. Res.* **2012**, *13*, 2171−2175.
(55) Harada, M.; Yamanaka, A.; Tanigaki, M.; Tada, Y. Mass and size effects on the transport properties of molten salts. *J. Chem. Phys.* **1982**, *76*, 1550−1556.
(56) Daivis, P. J.; Evans, D. J. Comparison of constant pressure and constant volume nonequilibrium simulations of sheared model decane. *J. Chem. Phys.* **1994**, *100*, 541−547.
(57) Hansen, J.-P.; McDonald, I. R. *Theory of simple liquids: with applications to soft matter*; Academic Press, 2013.
(58) Mukherji, S.; Brahma, D.; Balasubramanian, S. Modeling High Concentration Bisalt-in-Sulfolane Electrolytes and the Observation of Ligand-Bridged Cation-Pair Complexes. *J. Phys. Chem. B* **2024**, *128*, 10675−10687.
(59) Shao, Y.; Gudla, H.; Mindemark, J.; Brandell, D.; Zhang, C. Ion transport in polymer electrolytes: Building new bridges between experiment and molecular simulation. *Acc. Chem. Res.* **2024**, *57*, 1123−1134.

https://doi.org/10.1021/acs.jpcb.5c02097
J. Phys. Chem. B XXXX, XXX, XXX−XXX